Contrib Mineral Petrol (2008) 156:439–451
DOI 10.1007/s00410-008-0295-z

ORIGINAL PAPER

Aluminum-dependent trace element partitioning in clinopyroxene

Don Francis · William Minarik

Received: 16 May 2007 / Accepted: 3 March 2008 / Published online: 28 March 2008

Abstract As technical advances have dramatically increased our ability to analyze trace elements, the need for more reliable data on the compositional dependence of trace element partitioning between minerals and melt has become increasingly important. The late-Cretaceous Carmacks Group of south central Yukon comprises a succession of primitive high-Mg ankaramitic lavas characterized by shoshonitic chemical affinities and containing large complexly zoned clinopyroxene phenocrysts. The compositional zonation of the clinopyroxene phenocrysts is characterized by relatively Fe-rich ($Mg^{\#} = Mg/(Mg + Fe) = 0.85$), but mottled, cores surrounded by mantles of cyclically-zoned clinopyroxene whose $Mg^{\#}$ varies repeatedly between 0.9 and 0.80. These cyclically zoned clinopyroxene mantles appear to record the repeated influx and mixing of batches of primitive with more evolved magma in a deep sub-crustal ($\sim$1.2 GPa) magma chamber(s). Laser ablation ICP-MS was used to analyze the trace element variation in these zoned clinopyroxenes. The results indicate more than a threefold variation in the absolute concentrations of Th, Zr, rare earth elements (REE), and Y within individual clinopyroxene phenocrysts, with no apparent change in the degree of REE or high field strength element (HFSE) fractionation. The variation in absolute abundances of trace elements correlates closely with the major element composition of the clinopyroxene, with the most enriched clinopyroxene having the lowest $Mg^{\#}$ and highest Al contents. The problem is that the amount of crystal fractionation required to explain the major element variation ($\sim$20%) in these clinopyroxene phenocrysts cannot explain the increase in the abundance of the incompatible trace elements, which would require more than 70% crystal fractionation, if constant partition coefficients are assumed. The anomalous increase in incompatible trace elements appears to reflect an increase in their partition coefficients with increasing Al^{IV} in the clinopyroxene; with an increase in Al_2O_3 from 1.5 to 4.0 wt.% during $\sim$20% crystal fractionation over a temperature decrease of $\sim$100°C being associated with more that a threefold increase in the partition coefficients of Th, Zr, REE, and Y. The magnitude of these increases may indicate that the substitution of these trace elements into clinopyroxene is better modeled in some natural systems by a local charge balance model, rather than the distributed charge model that better replicates the results of annealed experiments. These findings indicate that the effect of Al on the partition coefficients of incompatible trace elements in clinopyroxene may be under appreciated in natural magmatic systems and that the application of experimentally determined clinopyroxene partition coefficients to natural systems must be done with caution.

Keywords Clinopyroxene · Trace element partitioning · Aluminum · Ankaramite · Carmacks · Phenocryst

Introduction

Our relatively recent ability to obtain reliable analyses of trace elements at increasing lower abundance levels is fuelling an accelerated use of trace elements in the evaluation of petrogenetic models. We have arrived at a point where the quality of analytical data rivals our understanding of the

Communicated by J.Blundy.

D. Francis (✉) · W. Minarik
Earth and Planetary Sciences, McGill University,
GEOTOP UQAM-McGill, Montreal, QC,
Canada H3A 2A7
e-mail: donf@eps.mcgill.ca

partitioning of trace elements between minerals and melt. The initial allure offered by trace elements—that their partition coefficients would be approximately constant at any P and T, with little compositional dependence—has slowly tarnished and now a wide range of values are quoted for the partition coefficients of many trace elements. The art of using trace elements to constrain petrogenetic models now lies in choosing appropriate values and compositional dependence. Recently, the seminal work of Blundy and Wood (2003, 1994) and Wood and Blundy (1997, 2001) in the application of lattice-strain and columbic potential models to predicting partition coefficients has greatly improved our understanding of the crystal chemical controls on the behaviour of trace elements in plagioclase and clinopyroxene, in particular. Not only does their model offer an effective tool with which to predict appropriate trace element partition coefficients based on mineral chemistry, their work has also highlighted the importance of taking into account the variation in trace element partition coefficients during petrogenetic processes caused by the effects of changing mineral composition (Blundy et al. 1998; Blundy and Wood 1991).

Here, we present the results of a study of the trace element zonation in clinopyroxene phenocrysts from an ankaramitic tuff horizon in the late-Cretaceous Carmacks Group of the south central Yukon. Our in situ laser-ICP study of cyclic growth zoning in clinopyroxene phenocrysts indicates that there is strong Al dependence in the clinopyroxene-melt partition coefficients for Zr, Th, the rare earth elements (REE), Y, and Fe^{3+}. We show that the partition coefficients for many of these elements appear to increase by a factor of more than 3 over as little as 20% crystal fractionation, as Al_2O_3 increases in clinopyroxene over a temperature interval of approximately 100°C. Although an effect of tetrahedrally-coordinated Al (Al^{IV}) in clinopyroxene on trace element partition coefficients has been predicted (Wood and Blundy 2001), our results suggest that the magnitude of this effect appears to be under appreciated in natural magmatic systems. The best models for the Al dependence of clinopyroxene-melt trace element coefficients (Hill et al. 2000; Wood and Blundy 1997, 2001) do not reproduce the variations we observe. We propose that this discrepancy might reflect a bias for local charge balance during crystal growth, because of the ease of attachment of 3^+ cations in octahedrally coordinated M2 sites adjacent to Al^{IV}, versus a bias for distributed charge balance in annealed experiments designed to achieve equilibrium.

Geological setting

The late-Cretaceous (69 Ma) Carmacks Group comprises an extensive volcanic province in the south central Yukon characterized by shoshonitic chemical affinities (Johnston et al. 1996). All the lavas of the Carmacks Group are relatively potassic, with calc-alkaline trace element signatures, including; enrichment in large ion lithophile and light rare earth elements (LREE), relative depletion in high field strength elements HFS, and flat heavy REE (HREE) patterns. The Carmacks volcanics erupted after the assembly of the diverse terranes that make up the northern Canadian Cordillera, and lies astride the transition from the Stikinia and Cache Creek Terranes of the Intermontane Belt in the South to the Yukon—Tanana Terrane in the North (Fig. 1). Although the beds of the Carmacks group are typically undeformed and sub-horizontal, there are significant paleo-topographic effects in some Carmacks volcanic units and attitudes have also been affected by post-volcanic slumping and regional warping.

The stratigraphy of the Carmacks Group (Fig. 2) has been traditionally divided into two in the central Carmacks area (Bostock 1936). There, the Lower Carmacks consists of a thick (600^+ m) sequence of agglomeratic and tuffaceous volcanoclastics, interbedded with small flows, all dominantly of andesitic composition, along with minor flows of dacite. The three thickest sections occur at Miller's Ridge, in the type Wolverine Creek area, and at Prospectors Mountain, which is cored by a small granite stock, suggesting that Lower Carmacks volcanism occurred at a series of localized strato-volcanic complexes. In contrast, the Upper Carmacks is dominated by a 500 m succession more effusive olivine and clinopyroxene-phyric basalt flows (5–10 m) that form a dissected regional plateau, and are not easily assigned to any individual central vent. The transition between the Upper and Lower Carmacks is marked by $\sim$100 m sequence of interbedded ash layers and thin flows, both consisting of porphyritic ankaramitic basalt (Figs. 2, 3).

Petrography and chemistry

Although the Carmacks volcanics have been extensively weather and oxidized, and the effects of zeolite-facies metamorphism are evident in the presence of amygdules filled with silica and/or carbonate, fresh samples can easily be obtained in which primary igneous mineralogy is well preserved. The Carmacks Group volcanics constitute a typical shoshonitic calc-alkaline suite, ranging in composition from primitive Mg-rich ankaramitic basalts, which are compositionally equivalent to the type absarokites of Wyoming (Gest and McBirney 1979), to more abundant shoshonitic andesites, and minor dacitic lavas. Although both the Upper and Lower Carmacks contain primitive ankaramites, the lower Carmacks is characterized by the greater abundance of pyroclastic rocks and more evolved lavas such as andesites and dacites. There is an increase in MgO up section in the lower Carmacks to a distinct spike

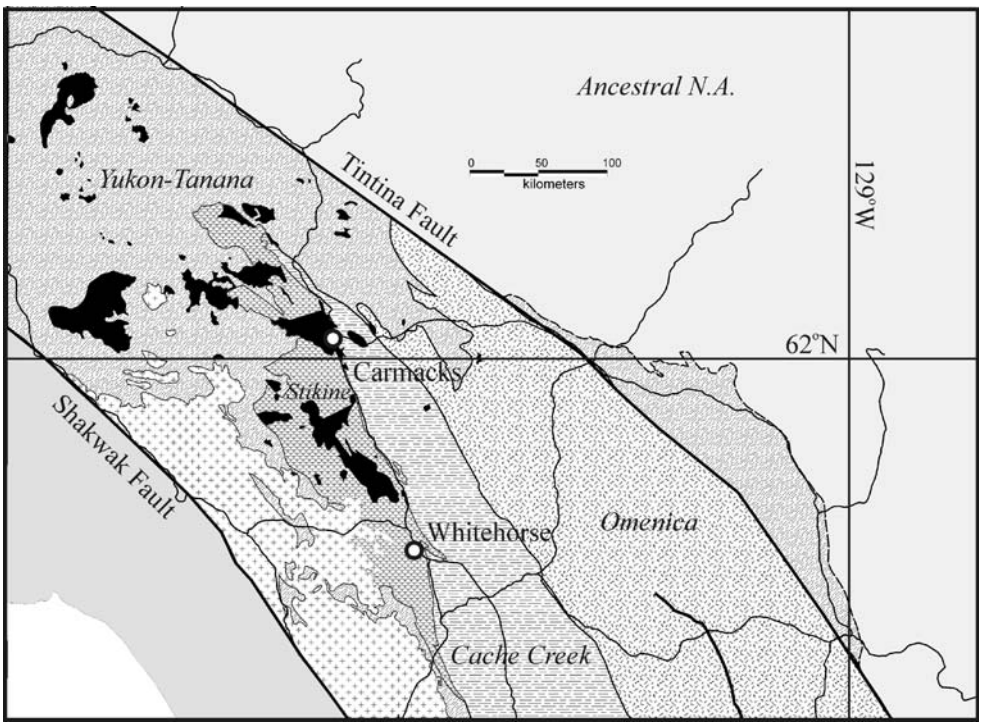

Fig. 1 Regional map showing the location of the Carmacks group volcanics (*black*) with respect to the towns of Whitehorse and Carmacks (*open circles*) and the accreted terranes (*italicized names*) of the northern Canadian Cordillera. The Miller's Ridge section in Figs. 2, 3 is located 5 km west of the town of Carmacks. The *thin black lines* represent the road system

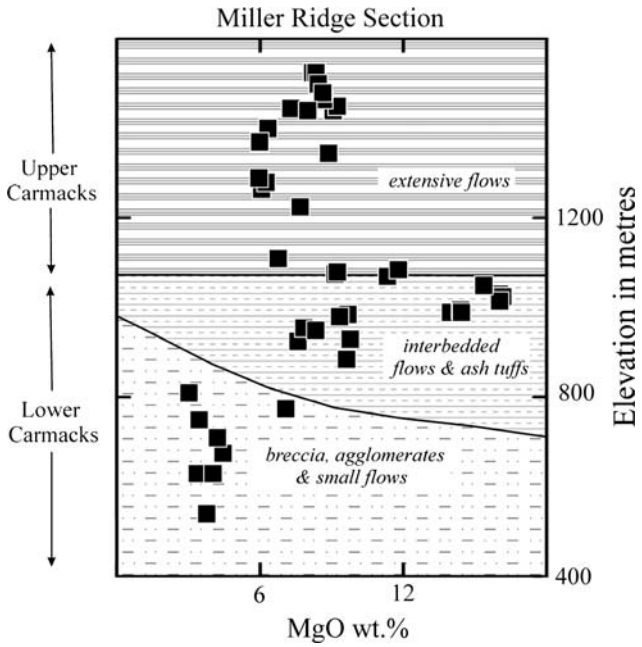

Fig. 2 Carmacks Group stratigraphy of Miller's Ridge, northwest of the Carmacks town site. *Black squares* represent the whole rock Mg contents of massive lava samples plotted against stratigraphic height

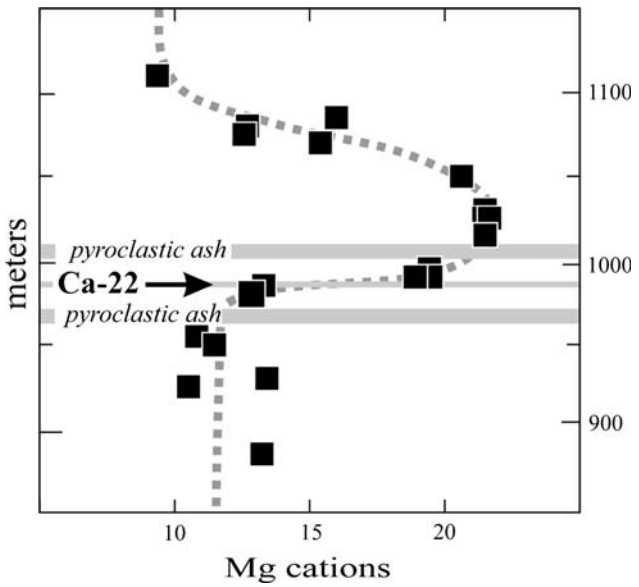

Fig. 3 Detailed stratigraphy at the transition between the Lower and Upper Carmacks lavas in the Miller's Ridge section showing the variation in whole rock Mg content with stratigraphic height and the position of ash sample CA-22 from which the clinopyroxenes of this study were extracted

of ~16 wt.% MgO at the transition to the Upper Carmacks (Fig. 3). The clinopyroxene phenocrysts analyzed for trace elements in this study were collected from an ankaramitic crystal tuff bed (4 m in thickness) interbedded with the ankaramite flows at the transition between the Lower and Upper Carmacks (Fig. 3).

The massive flows in the interval shown in Fig. 3 range in composition from primitive ankaramite (~16 wt. MgO) to basalt with 8 wt.% MgO (Table 1), but there is a distinct gap at approximately 12–13 wt.% MgO. The most magnesian ankaramites in this interval contain abundant olivine and lesser clinopyroxene phenocrysts (~20%) in a matrix

Table 1 Whole rock compositions of the lavas across the transition from the Lower to Upper Carmacks Group in Fig. 3, listed in order of decreasing stratigraphic height

# Meters	CA-11 1025	CA-12 1015	CA-13 995	CA-14 990	ML-20 990	CA-15 985	CA-16 980	CA-17 955	CA-18 950	ML-17 885
SiO_2	50.1	49.95	50.51	50.55	50.68	52.11	51.86	52.86	52.82	52.29
TiO_2	0.7	0.68	0.75	0.74	0.77	0.82	0.8	0.94	0.93	0.91
Al_2O_3	10.72	10.78	11.16	10.88	11.16	12.19	12.38	13.62	13.39	12.74
Cr_2O_3	0.15	0.15	0.13	0.13	0.13	0.08	0.08	0.06	0.06	0.08
FeO	7.65	7.5	7.82	7.93	7.96	7.89	7.77	7.57	8.01	8.21
MgO	15.84	15.57	14.06	14.11	13.68	9.47	9.07	7.69	8.24	9.51
MnO	0.15	0.12	0.15	0.14	0.15	0.15	0.15	0.14	0.14	0.15
CaO	6.36	6.18	6.95	7.12	7.29	8.73	8.87	8.3	8.4	8.51
Na_2O	2.22	2.19	2.18	2.28	2.16	2.6	2.58	2.88	2.97	2.58
K_2O	2.96	2.88	2.89	2.80	2.85	2.58	2.43	2.70	2.64	2.60
P_2O_5	0.45	0.45	0.45	0.43	0.43	0.42	0.41	0.45	0.44	0.42
LOI	1.91	2.25	2.66	2.25	2.04	2.26	2.81	2.58	1.59	1.48
Total	99.22	98.71	99.71	99.36	99.29	99.3	99.21	99.79	99.63	99.47
Rb	81.5	74.9	72.6	66.3	66.9	61.6	57.7	60.0	58.1	61.4
Ba	1451.0	1405.0	1482.0	1476.0	1576.0	1520.0	1516.0	1629.0	1618.0	1601.0
Sr	498.1	484.6	466.1	484.3	506.0	597.0	600.6	637.2	644.8	598.3
Y	16.4	16.9	18.1	18.3	18.5	19.5	19.2	21.1	21.0	19.8
Zr	110.5	112.0	117.8	116.3	118.7	130.4	127.8	143.4	140.5	125.7
Nb	8.7	9.1	9.6	9.3	9.4	8.5	8.6	9.4	9.2	8.3
Ta	0.44	0.46	0.43	0.45	0.00	0.48	0.47	0.51	0.51	0.00
Hf	2.60	2.80	2.60	2.70	3.70	3.40	3.30	3.40	3.40	1.50
Ni	561.5	553.0	438.0	440.0	431.5	119.5	115.0	117.0	124.0	175.0
Pb	8.10	19.00	–	12.00	8.83	12.30	6.00	15.00	17.00	7.30
Th	4.44	4.92	4.08	4.35	8.50	4.62	5.02	4.75	4.63	5.21
U	1.37	1.41	1.17	1.27	5.43	1.22	1.14	1.34	1.29	1.67
La	24.30	24.70	23.30	23.20	22.67	26.80	22.10	28.20	28.10	24.73
Ce	47.20	48.80	47.00	46.30	45.03	53.60	44.60	56.40	56.80	49.37
Nd	19.80	20.50	19.70	19.90	22.57	23.20	21.10	24.30	24.70	25.10
Sm	4.54	4.51	4.51	4.48	4.26	5.12	4.46	5.54	5.61	5.13
Eu	1.15	1.16	1.14	1.15	1.39	1.30	1.27	1.46	1.46	1.70
Gd	3.51	3.59	3.53	3.57	4.40	4.08	4.07	4.35	4.40	4.80
Tb	0.59	0.59	0.60	0.61	0.53	0.71	0.62	0.74	0.75	0.65
Dy	2.90	3.04	3.11	3.11	2.88	3.61	3.28	3.84	3.90	3.87
Ho	0.52	0.54	0.56	0.56	0.66	0.65	0.62	0.71	0.72	0.79
Er	1.46	1.51	1.53	1.57	1.57	1.86	1.76	2.01	2.02	1.89
Tm	0.20	0.21	0.22	0.22	0.28	0.27	0.24	0.29	0.29	0.38
Yb	1.19	1.28	1.35	1.35	1.43	1.60	1.55	1.71	1.77	1.55
Lu	0.18	0.19	0.20	0.21	0.23	0.24	0.24	0.26	0.27	0.24

Alteration-free samples were crushed in a steel jaw crusher and then ground in an alumina shatter box. The major elements, along with Cr, Ni, Co, and V, were analyzed on fused beads prepared with lithium tetraborate with a Phillips PW2400 4 kW automated XRF spectrometer using an α-coefficient correction technique. Precision is estimated to be better than 0.5% for Si and better than 1% for all other major elements. The trace elements Rb, Sr, Zr, Nb, and Y were also determined by XRF, but on 40 mm diameter pressed pellets prepared with Hoechst Wax C Micro powder. The REE, Th, and other trace elements were analyzed by inductively coupled plasma mass spectrometry, using a Perkin Elmer Sciex Elan 6100 ICP-MS at Activation Laboratories and a lithium metaborate/tetraborate fusion digestion. Precision is estimated to be less than 5%

of plagioclase (An 55), K-feldspar (Or 60), and clinopyroxene. The size and abundance of clinopyroxene relative to olivine phenocrysts increases dramatically in the lavas with decreasing whole-rock MgO. The appearance of clinopyroxene mantles on olivine phenocrysts indicate the existence of an olivine reaction relationship in magmas

with compositions below ~9 wt.% MgO, at approximately the same point at which feldspar first becomes a phenocryst phase, along with olivine and clinopyroxene.

Compositional zoning in clinopyroxene phenocrysts

Both the olivine and clinopyroxene phenocrysts in the ankaramitic lavas and the interbedded ash in this stratigraphic interval are strongly zoned, but commonly in a contrary sense. The olivine phenocrysts typically exhibit normal zoning (Fig. 4a), commonly displaying skeletal outer margins. The most magnesian cores retain compositions up to Fo 93, but range down to Fo 83 in adjacent rims, with a concomitant decrease in Ni. An absence of deformation lamellae and relatively high Ca contents (CaO > 0.3 wt.%) indicate that these olivines represent cognate phenocrysts rather than mantle xenocrysts.

The clinopyroxene phenocrysts, on the other hand, exhibit more complex zoning patterns that, overall, are characterized by cyclically-zoned magnesian-rich mantles developed on mottled, vuggy, and more Fe-rich cores (Figs. 4b, 5). The clinopyroxene phenocrysts of the Carmacks ankaramites straddle the boundary between endiopside and augite in the pyroxene quadrilateral, if all the Fe is calculated as Fe^{2+}, with magnesian numbers ($Mg^{\#} = Mg/(Mg + Fe)$) ranging from ~0.90 down to 0.78, associated with a concomitant increase in Al_2O_3 from 1.5 to 4.0 wt.%. Notably, the range of compositions observed within individual clinopyroxene phenocrysts of this study spans the range of clinopyroxene compositions obtained for Carmacks lavas as a whole, with the difference that there is a marked compositional gap at a $Mg^{\#}$ of ~0.85 (assuming all Fe as Fe^{2+}) in the individual phenocryst data in this stratigraphic interval. The cores of the clinopyroxene phenocrysts are relatively Fe-rich ($Mg^{\#}$ 85), but are compositionally heterogeneous and appear mottled in backscattered electron images (Figs. 4, 5), suggesting the irregular replacement of relatively Mg-rich clinopyroxene by more Fe-rich clinopyroxene. Surrounding the cores are mantles of cyclically zoned clinopyroxene with $Mg^{\#}$'s ranging from 0.90 to 0.80 more than three times (Figs. 5, 6) across their width. In each cycle, as MgO in the clinopyroxene decreases from 18 to 15 wt.%, Al_2O_3 and Na_2O increase from 1.5 to 4 wt.% and from 0.3 to 0.4 wt.%, respectively (Table 2, Fig. 7), and there is an increase in the fraction of Fe^{3+} ($Fe^{3+}/\sum Fe$) calculated by stoichiometry from 0.2 to 0.3, shifting the majority of the clinopyroxene

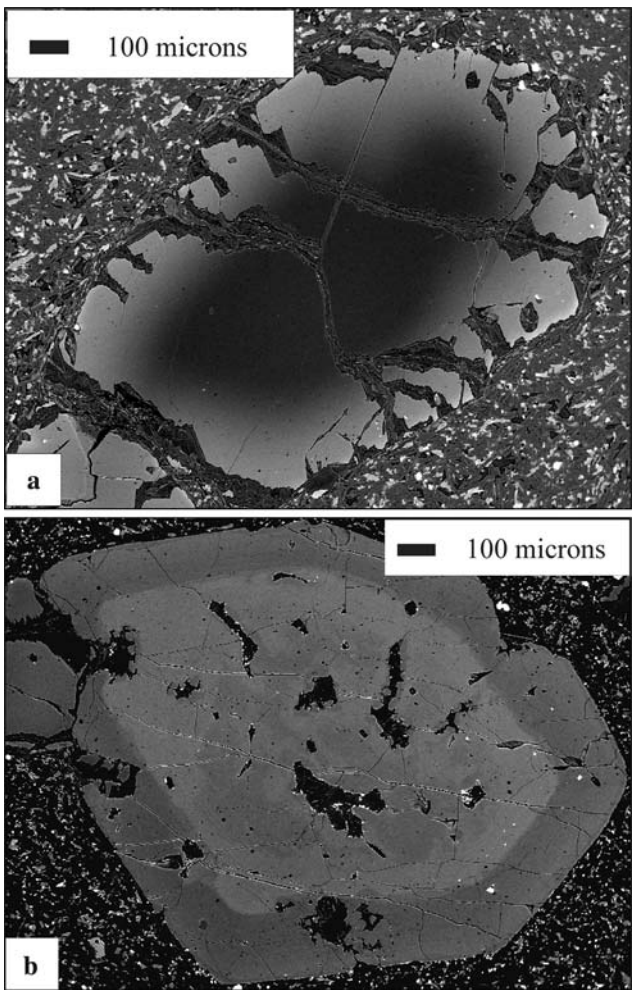

Fig. 4 **a** Back-scattered electron image showing the normal zoning exhibited by an olivine phenocryst, with a darker more Mg-rich rim and a brighter more Fe-rich core. **b** Back-scattered electron image showing reversed zoning in a clinopyroxene phenocryst, with a darker more Mg-rich margin on a brighter more Fe-rich mottled and vuggy core

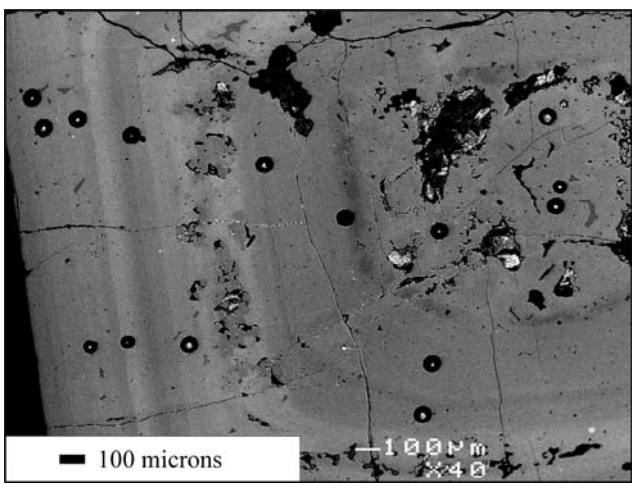

Fig. 5 Detailed back-scattered electron image of the cyclic zoning in the mantle of an analyzed clinopyroxene phenocryst with the laser oblation pits showing as *black spots*. Brightness is inversely proportional to $Mg^{\#}$

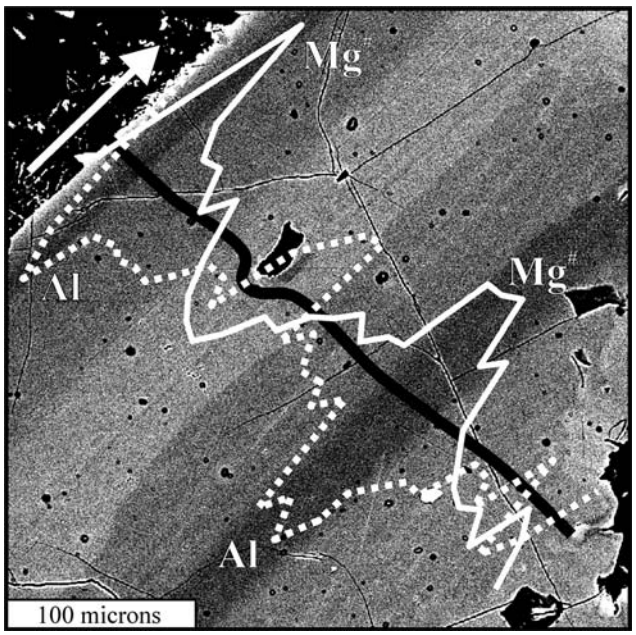

Fig. 6 Detailed back-scattered electron image of cyclic zoning in the mantle of a clinopyroxene phenocryst with the variation in $Mg^{\#}$ (*solid white line*), Al content (*dotted white line*), and the location of the analyzed transect (*solid black line*) superimposed. The *white arrow* indicates the direction of increasing $Mg^{\#}$ and Al content

analyses into the endiopside field of the pyroxene quadrilateral. The variations in the concentrations of Sr, Th, Zr, REE, and Y across four of these zoned clinopyroxene phenocrysts were determined with a laser ablation ICP-MS. We used a NewWave UP-213 system coupled to a Perkin-Elmer Elan DRCplus ICP-MS run in standard mode. The 213 nm ultraviolet laser ablated a 60 μm spot with ~10 J/cm^2 energy density into a helium cell gas. Data was reduced with the Glitter program using both ^{29}Si and ^{43}Ca as ratioing isotopes. The results (Table 2) indicate that there is an excellent correlation between trace element abundances and the major element composition of the clinopyroxene, with Zr, Th, REE, and Y increasing by more than a factor of 3, as Al^{IV} increases from 0.04 to 0.16 atoms per formula unit (Figs. 8, 9, 10a). In comparison, the concentration of Sr increases by only ~20% (Fig. 8a). These variations are cyclically repeated in each successive cycle of the zoned clinopyroxene mantles. Despite the large range in absolute concentrations of incompatible trace elements in the zoned clinopyroxene phenocrysts, however, there is essentially no relative fractionation of the REE (Figs. 10b, 11) or high field-strength elements (HFSE).

Discussion

The clinopyroxenes of this study come from an ash layer within the stratigraphic transition between the Upper and Lower Carmacks, and coincides with a prominent spike in the MgO content in the succession of ankaramitic lavas. The contrasting $Mg^{\#}$ zoning profiles of olivine and clinopyroxene phenocrysts in these ankaramitic lavas suggests that they represent a mixed population of phenocrysts recording the blending of primitive picritic magma with a more evolved ankaramitic magma. This interpretation is supported by the compositional gap in the cyclically zoned clinopyroxenes at a $Mg^{\#}$ of ~0.85, and in the lavas at ~10 wt.% MgO. The clinopyroxene phenocrysts apparently record the repeated influx and mixing of at least three successive batches of primitive picritic magma. The ratio of octahedrally coordinated Al (Al^{VI}) to tetrahedrally-coordinated Al (Al^{IV}) is less than 1 in all the clinopyroxene analyses, but an application the jadeite-diopside/hedenbergite barometer (Putirka et al. 1996, 2003) using the compositions of the ankaramitic lavas as the liquid compositions suggests that the magma chamber in which this mixing occurred was relatively deep (~1.2 ± 0.1 GPa), possibly at the crust-mantle interface.

The problem with the foregoing scenario is the magnitude of the increase in the levels of Th, Zr, REE, and Y observed with increasing Al in the zoned clinopyroxene phenocrysts of the Carmacks ankaramites. The concentrations of these incompatible trace elements repeatedly rise by a factor of more than three within individual cycles of the clinopyroxene mantles, without any relative fractionation between trace elements, or any evidence of anomalous behaviour of these trace elements in the ankaramitic lavas which span this stratigraphic interval. In order to better constrain the possible origin of these "anomalous" trace element variations in the Carmacks clinopyroxene phenocrysts, we constructed a computer model for the Carmacks magmas that calculated the compositions of liquid, olivine, and clinopyroxene during crystal fractionation. An average of 7 magnesian ankaramitic lavas (MgO = 15.8 wt.%) was used as a parent magma, and crystal fractionation was simulated by removing olivine and then olivine and clinopyroxene in instantaneous equilibrium with the liquid in steps of 0.1% (see explanation of Fig. 12 for further details). Olivine began to crystallize in the model at ~1,420°C. After the fractionation of ~12 wt.% olivine, the point at which clinopyroxene joined olivine as a crystallizing phase (MgO ~ 12 wt.%, 1,350°C) was determined by matching the maximum $Mg^{\#}$ observed in the clinopyroxene phenocrysts with that predicted by the model by trial and error, and coincides with an inflection in the array of whole rock lava data (Fig. 12). The proportions of olivine and clinopyroxene removed (45:55) were adjusted to best reproduce the anti-variation between Mg and Al in the Carmacks lavas. The results of this modeling indicate that the variation in $Mg^{\#}$ and Al observed within each cycle of the mantles of the clinopyroxene phenocrysts is well

Table 2 Selected major and trace element analyses across two zoned Carmacks clinopyroxene phenocrysts in ankaramitic ash sample Ca-22, in each case listed in order of increasing Al content

	CPX-22-2					CPX-22-3				
#	11	18	24	23	2	10	9	5	18	17
SiO_2	53.93	53.29	52.26	51.79	50.55	53.42	52.91	51.90	50.96	50.21
TiO_2	0.18	0.37	0.51	0.61	0.86	0.21	0.41	0.48	0.67	0.93
Al_2O_3	1.21	1.90	2.96	3.96	4.43	1.69	2.28	2.65	3.62	4.95
Cr_2O_3	0.49	0.48	0.50	0.33	0.30	0.77	0.40	0.29	0.58	0.27
FeO	4.23	4.74	5.88	6.24	7.00	4.60	6.10	6.61	5.94	7.57
MgO	18.24	17.30	16.86	16.12	15.42	18.17	17.48	16.52	15.92	15.10
MnO	0.13	0.13	0.16	0.15	0.16	0.14	0.18	0.17	0.14	0.17
CaO	21.41	21.95	20.86	20.82	20.82	20.72	20.37	20.43	21.60	20.40
Na_2O	0.28	0.29	0.37	0.42	0.40	0.38	0.32	0.32	0.34	0.45
K_2O	0.00	0.00	0.00	0.00	0.00	0.00	0.00	0.01	0.00	0.01
Total	100.10	100.46	100.37	100.45	99.95	100.09	100.44	99.39	99.77	100.05
Ba	1.54	0.8	0.6	3.66	0.91	2.25	4.21	0.213	0.073	0.233
Sr	60.4	72.1	82.1	96.4	94.0	59.9	71.8	74.6	89.4	87.9
Y	3.9	9.6	14.2	18.5	24.8	5.6	11.4	13.9	17.2	25.9
Zr	3.0	10.3	20.5	26.2	43.3	4.1	11.6	19.1	29.4	46.1
Nb	0.018	0.035	0.030	0.098	0.084	0.035	0.078	0.034	0.081	0.104
Ta	0.013	0.035	0.020	0.025	0.022	0.010	0.003	0.010	0.019	0.014
Hf	0.144	0.435	1.050	1.210	1.970	0.240	0.384	0.782	1.270	2.040
Pb	0.047	0.319	0.099	0.162	0.129	0.488	0.376	0.133	0.076	0.128
Th	0.0120	0.0231	0.0231	0.0580	0.0580	0.0000	0.0420	0.0149	0.0390	0.0740
U	0.0035	0.0172	0.0070	0.0101	0.0119	0.0189	0.0074	0.0089	0.0254	0.0138
La	0.74	1.58	2.53	3.20	4.37	0.82	1.74	2.56	3.22	4.43
Ce	2.40	5.36	8.89	11.13	16.12	3.03	6.28	9.09	11.20	15.63
Nd	2.64	5.53	10.06	13.01	17.22	3.85	7.45	10.08	12.63	17.57
Sm	0.76	1.73	3.41	4.36	5.44	1.08	2.48	3.09	3.94	6.00
Eu	0.28	0.52	0.97	1.23	1.72	0.42	0.78	1.00	1.18	1.55
Gd	0.96	2.34	3.35	4.28	6.03	1.55	2.75	3.72	3.81	6.16
Dy	0.77	1.99	2.97	3.91	5.21	1.10	2.44	2.77	3.93	5.39
Yb	0.16	0.79	1.15	1.59	2.03	0.42	0.83	1.47	1.61	2.18
Lu	0.04	0.10	0.18	0.24	0.29	0.09	0.14	0.11	0.17	0.29

The major elements were determined with a JEOL 8,900 electron microprobe using an accelerating voltage of 15 kV and a beam current of 20 nanoamps, with counting times of 20 s on peak and background for most elements. Natural and synthetic standards were used for calibration with a JEOL supplied ZAF correction procedure. The trace element analyses were performed with a NewWave 213 nm laser, with a 60 μm spot size and an energy density of $\sim$10 J/cm^2 energy density, combined with a PerkinElmer Elan DRCplus ICP-MS

reproduced by approximately 20% crystal fractionation with a temperature decrease from 1,350 to 1,250°C. Over this range, the liquid composition decreases from 12 to 7 wt.% MgO, and the ratio of non-bridging oxygens to tetrahedral cations (NBO/T) increases from 1.4 to 1.0.

The behaviour of Sr, which sits in the eight coordinated M2 crystallographic site of the clinopyroxene phenocrysts, is relatively well reproduced by the computer model (Fig. 8a), which used a constant partition coefficient for Sr (D_{Sr}) of 0.12, a typical value within the range of those quoted for Sr in clinopyroxene coexisting with basalt on the GERM web site (http://www.earthref.org/GERM). Serious problems arise, however, with the more incompatible trace elements Th, REE, and Y that also occupy the M2 site of clinopyroxene, and Zr, which occupies the octahedral M1 site. No model using reasonable constant partition coefficients (GERM web site) comes close to predicting the rise observed in these incompatible trace elements with increasing tetrahedrally coordinated aluminum (Al^{IV}) in the Carmacks clinopyroxene phenocrysts (Figs. 8, 9, 10a). The behaviour of Th (solid line, Fig. 8b) is, however, well modeled using an expression for the partition coefficient of Th (D_{Th}) that accounts for the effect of Al^{IV} on the occupancy of the clinopyroxene M2 site

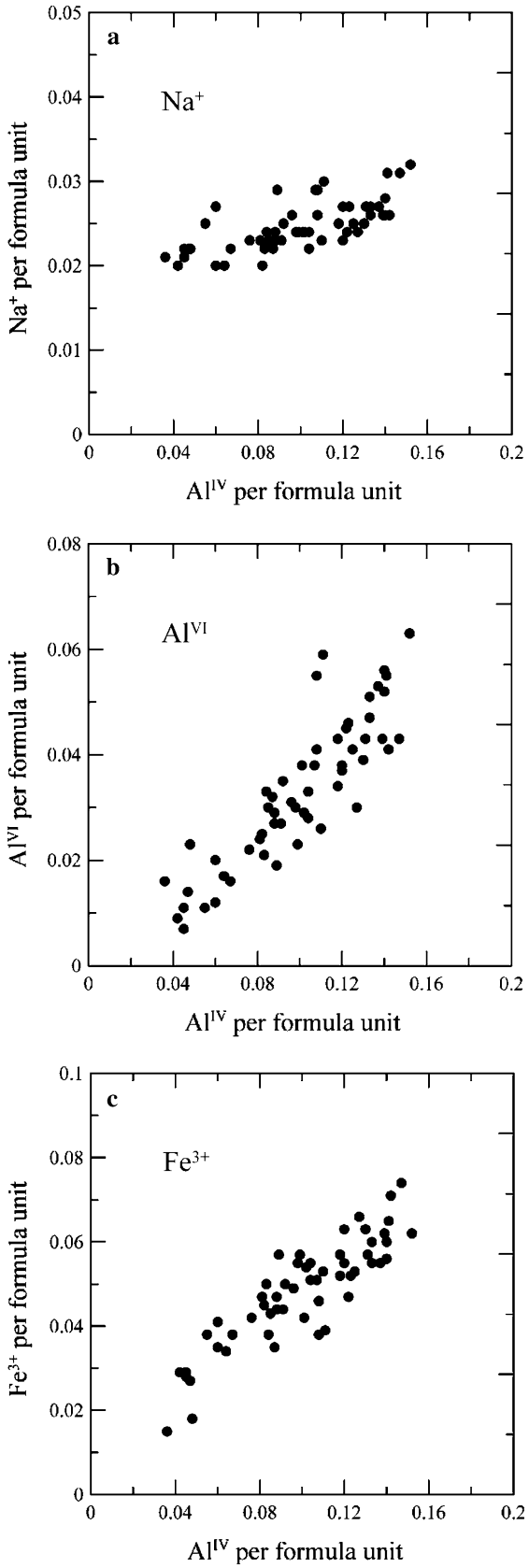

◀ **Fig. 7** Variation in Na^+, Al^{VI}, and Fe^{3+} with Al^{IV} in four different Carmacks clinopyroxene phenocrysts in ankaramitic ash sample CA-22. Al^{IV} and A^{IV} were calculated by normalizing the total number of cations to 4 and then taking $Al^{IV} = 2–Si$, and $Al^{VI} = Al–Al^{IV}$

(Lundstrom et al. 1994). The substitution of Al^{IV} increases the average charge on the M1 site because of the coupled solution of Al^{VI}, Fe^{3+}, and Cr^{3+}, thus facilitating the entry of highly charged cations like Th (Wood and Trigila 2001) into the M2 site. The success of the crystal fractionation model in reproducing the rise in Th with Al^{IV} in the Carmacks clinopyroxene phenocrysts indicates that the behaviour of Th is not anomalous and therefore consistent with approximately 20% crystal fractionation. More significantly, it raises the possibility that the apparently anomalous behaviours of Zr, REE, and Y may also reflect compositional effects on their partitioning into clinopyroxene. The existing experimental data do support an increase in the partition coefficients for Zr (Forsythe et al. 1994; Lundstrom et al. 1994) and REE in clinopyroxene (Wood and Blundy 2001; Wood and Trigila 2001) with increasing Al^{IV}. Contrary to the case for Th, however, the smaller Zr^{4+} ion occupies the octahedrally coordinated M2 site in clinopyroxene and its entry appears to be favoured by charge compensation involving both the coupled substitution of Al^{3+} for Si^{4+} in tetrahedral coordination (Wood and Trigila 2001) and Na^+ for Ca^{2+} in the M2 site (NaZrAlSiO6) (Lundstrom et al. 1994). The dashed line in Fig. 8c shows the calculated increase in Zr in clinopyroxene produced by the crystal fractionation model using a constant D_{Zr} of 0.1, a typical value from the GERM Website, cannot reproduce the Zr variation. A number of authors have demonstrated an Al^{IV} dependence to D_{Zr} and the dot–dash line in Fig. 8c shows the calculated increase in Zr using an expression for the Al^{IV} dependence of D_{Zr} $\left(10^{(-1.7+4.4\times Al_{IVcpx})}\right)$ derived from a data compilation of Wood and Trigala (2001). Clearly, models with a reasonable constant partition coefficient and models using a partition coefficient whose dependence on Al^{IV} is estimated from existing experimental results fall well short of reproducing the Zr variation observed clinopyroxene data. The solid arrow in Fig. 8c indicates the calculated increase in Zr in the Carmacks clinopyroxenes with increasing Al when the constant for Al^{IV} dependence in the preceding expression is arbitrarily adjusted to better fit the observed data $\left(D_{Zr} = 10^{(-1.7+11.5\times Al_{IVcpx})}\right)$

The substitution of REE in the M2 site of clinopyroxene is thought to be facilitated by two different components $(Na_{0.5}REE_{0.5})MgSi_2O_6$ and $(REE)MgAlSiO_6$ (Wood and Blundy 1997, 2001). In either case, the charge imbalance associated with the entry of a 3^+ REE cation into the M2 is

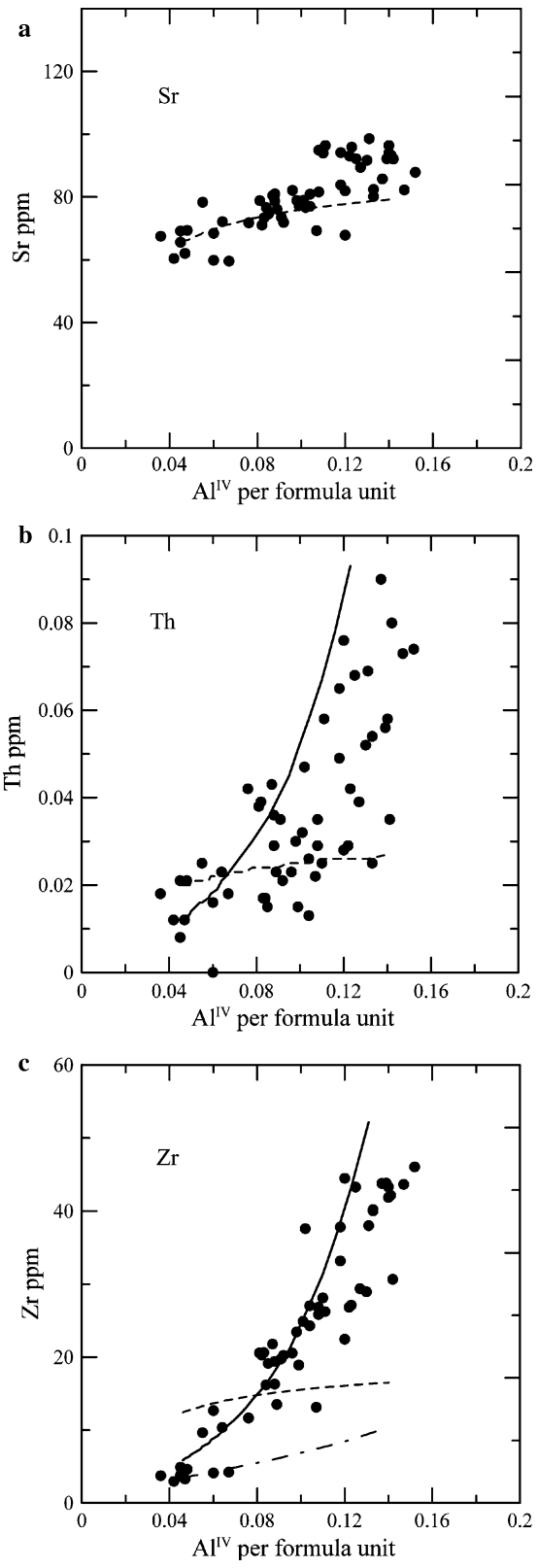

◀ **Fig. 8** **a** Sr, **b** Th, and **c** Zr versus Al^{IV} in four different Carmacks clinopyroxene phenocrysts in ankaramitic ash sample CA-22. The *dashed line* in Fig. 8a shows the Sr content of the clinopyroxenes calculated using a constant D_{Sr} of 0.12, taken from the GERM website. The *dashed line* in Fig. 8b shows the calculated Th content of clinopyroxene using a constant D_{Th} of 0.003, taken from the GERM website. The *solid line* in Fig. 8b shows the calculated Th content of clinopyroxene using the Al dependence algorithm for D_{Th} ($D_{Th} = 10^{(-3.1 + 11.5 \times AlIV)}$) of Lundstrom et al. (1994). The *dashed line* in Fig. 8c shows the Zr content of the clinopyroxenes calculated by the crystal fractionation model using a constant D_{Zr} of 0.1, taken from the GERM web site. The *dot–dash line* shows Zr calculated for clinopyroxene using a model for the Al dependence of D_{Zr} ($D_{Zr} = 10^{(-1.7 + 4.4 \times AlIV)}$) estimated from the compilation of Wood and Triglia (2001). The *solid line* in Fig. 8c shows calculated Zr using a model in which the constant for Al^{IV} in the preceding expression is adjusted to better fit the observed clinopyroxene data ($D_{Zr} = 10^{(-1.7 + 11.5 \times AlIV)}$)

facilitated by a coupled solid solution in which either Na^{1+} substitutes for Ca^{2+} in the M2 site, or Al^{3+} substitutes for Si^{4+} in the tetrahedral site. The increase in REE in the Carmacks clinopyroxene phenocrysts is associated with an increase in both Na and Al^{IV}. The variation in Na is, however, relatively small compared to that of Al^{IV} (Fig. 7) and the latter is a more likely explanation for the apparent anomalous behavior of the REE. The dashed lines in Fig. 9 show the calculated increase in selected REE in the Carmacks clinopyroxene using typical constant D's from the GERM Website. The dot–dash lines in Fig. 12 shows the rise in selected REE using the formalism of Wood and Bundy (1997), but with a value for D_o (the partition coefficient for a 3^+ cation whose radius equals the strain-free radius (R_o) of the M2 site) for the entry of 3^+ cations into the M2 site whose Al^{IV} dependence is taken from Wood and Blundy (2001), which assumes a distributed charge balance. The solid line shows the rise in model REE contents using a D_o whose Al^{IV} dependence is modeled after Wood and Blundy (2001) assuming local charge balance between REE^{3+} in the M2 site and adjacent Al^{IV} within clinopyroxene. Similarly, the dot–dash and solid lines in Fig. 10a show the calculated rises in Y, using D_o's whose Al^{IV} dependencies are calculated for distributed and local charge balance respectively. The local charge balance model for the Al^{IV} dependence of D_o clearly better reproduces the variation of REE and Y (Figs. 9, 10a) in comparison to both models using constant partitioning coefficients, and models in which the Al^{IV} dependency of D_o is calculated assuming distributed charge balance, despite the fact that the latter model better explains the experimental data (Wood and Blundy 2001).

The inability of experimentally calibrated models to reproduce the rise in many of the trace elements in the Carmacks clinopyroxene phenocrysts suggests that something else is at work. Gaetani (2004) has shown that melt structure may have a significant effect on the partitioning of trace elements into crystals. The magnitude of the effect of melt polymerization is proportional to the field strength (charge/radius) of the cation. The fact that the variation in

Sr^{2+} in the Carmacks clinopyroxene is relatively well reproduced by a model with a constant D is consistent with its low field strength, making it relatively insensitive to changing melt structure. The lack of fractionation among similarly charged cations, such as the REE and Y, despite an apparent three fold variation if their partition coefficients, would also be consistent with a melt polymerization effect. Significant effects of melt structure on trace element partitioning have, however, only been demonstrated at low ratios of non-bridging oxygens to tetrahedrally coordinated cations (NBO/T) (Gaetani 2004). The NBO/T ratios of the model Carmacks liquids, and their corresponding lavas, during the crystallization of clinopyroxene with olivine range from 1.4 to 1.0, as MgO decreases from 12 to 7 wt.% across the sampled stratigraphic interval. These NBO/T values are significantly larger than the value of $\sim$0.6, above which melt structure appears to have a relatively minor effect on trace element partitioning (Gaetani 2004).

An explanation for the apparent anomalous behaviour of highly charge cations in the Carmacks clinopyroxene phenocrysts might lie in the kinetics of crystal growth involving a finite boundary layer (Albarede and Bottinga 1972). If diffusion in the liquid boundary layer adjacent to a growing crystal face is slow with respect to crystal growth, then the crystal will become chemically zoned, with the greatest zonation exhibited by chemical components with the lowest diffusion coefficients, which would appear to exhibit partition coefficients that are higher than equilibrium values (Albarede and Bottinga 1972). In such an explanation, the cyclic nature of the chemical zonation in the mantles of the Carmacks clinopyroxenes would reflect the repeated development and then stagnation of a finite chemical boundary layer. The relative magnitude of this effect is also expected to be proportional to the field strength of the cation considered (Baker 1990), which is consistent with the relative magnitudes of the observed anomalous increases in the apparent partition coefficients: Th^{4+}, $Zr^{4+} > REE^{3+}$, $Y^{3+} > Sr^{2+}$. A number of features, however, argue against an interpretation of the trace element zonation observed in the Carmacks clinopyroxenes in terms of boundary layer kinetics. First, the contrasting zoning patterns of the olivine and clinopyroxene

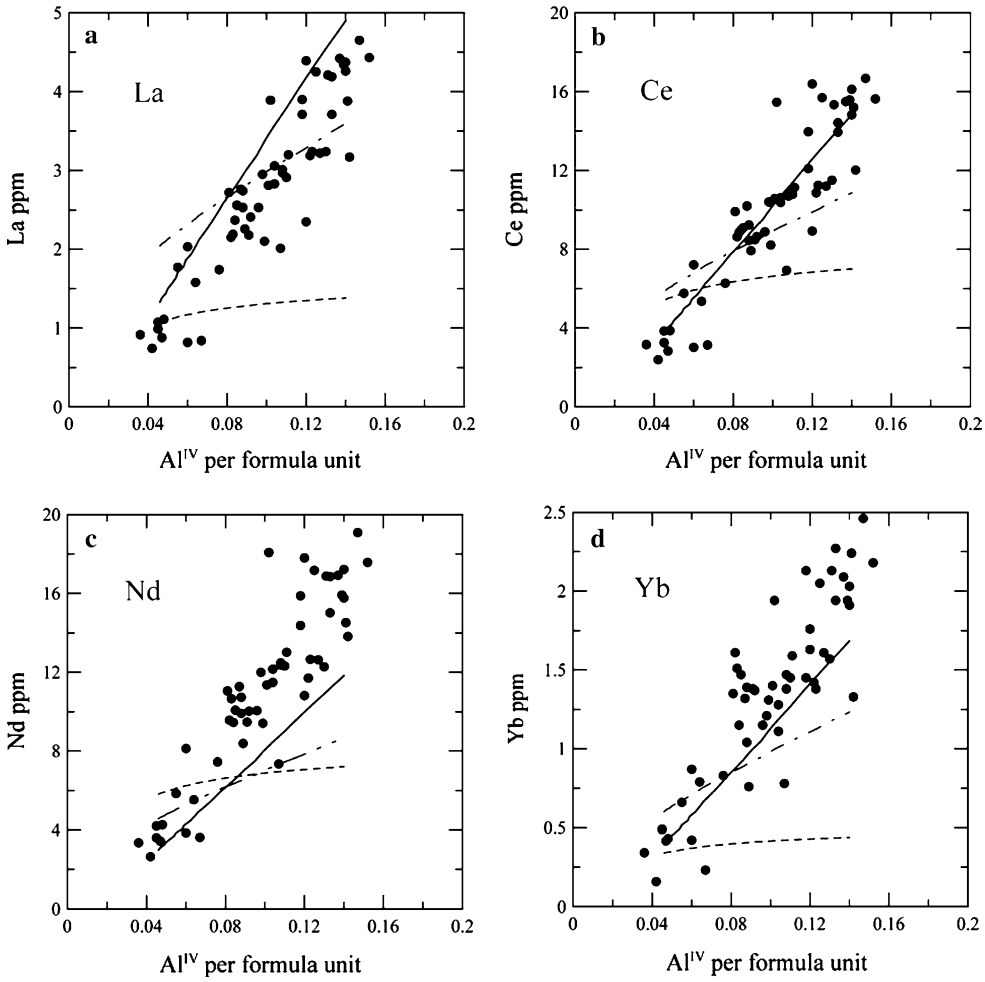

Fig. 9 Selected REE versus Al^{IV} in four different clinopyroxene phenocrysts from Carmacks ankaramitic ash sample CA-22. The *dashed lines* show the REE contents of the clinopyroxenes calculated by the crystal fractionation model using constant D_{REE}'s taken from the GERM website. The *dot–dash line* show the REE calculated for clinopyroxene using the Al dependence of D_o of Wood and Bundy (2001) assuming distributed charge balance, but an R_o of 1.01 rather than 1.045, which not only better fits the data, but is in agreement with the strain-free radius of the clinopyroxene M2 site obtained in the experimental results of Adam and Green (2006). The solid line shows the REE calculated for clinopyroxene using the Al dependence of D_o of Wood and Bundy (2001) assuming local charge balance with an R_o of 1.01

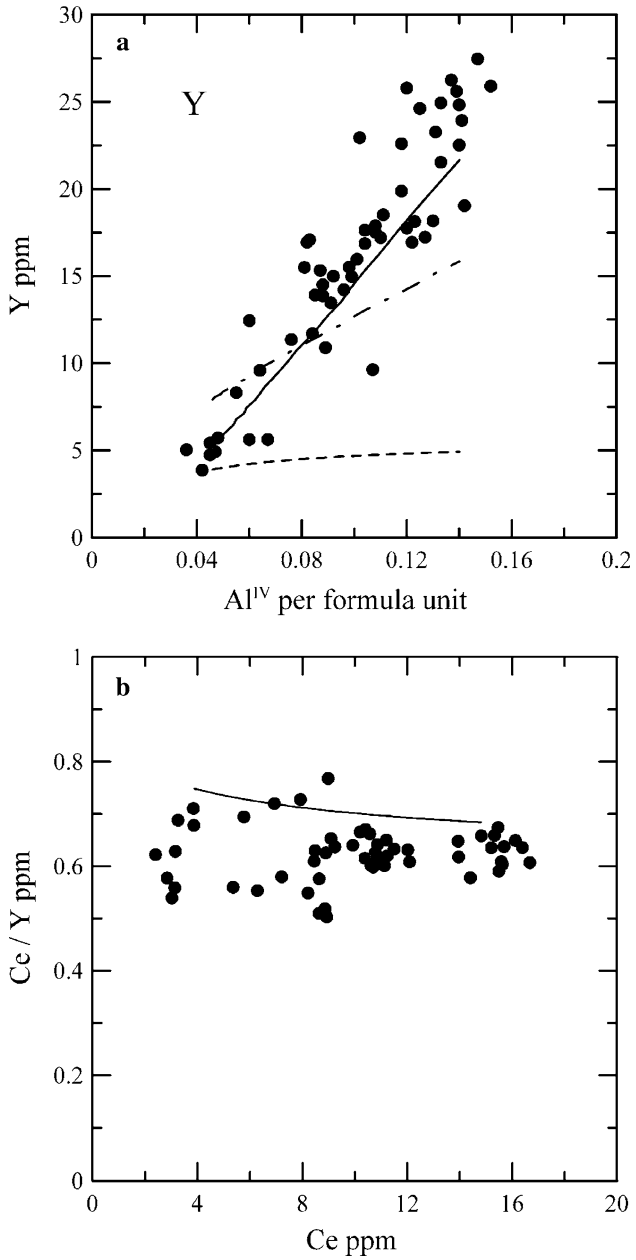

Fig. 10 **a** Y versus Al in four Carmacks clinopyroxene phenocrysts. The *dashed line* shows the Y contents calculated for clinopyroxenes by the crystal fractionation model using a constant D_Y of 0.2, taken from the GERM website. The *dot–dash line* show the Y calculated for clinopyroxene using the Al dependence of D_o of Wood and Bundy (2001) assuming distributed charge balance, but an R_o of 1.01 rather than 1.045. The *solid line* shows the Y calculated for clinopyroxene using the Wood and Bundy type model in Fig. 9 in which the Al dependence of D_o is calculated assuming local charge balance. **b** Ce/Y versus Ce in four Carmacks clinopyroxene phenocrysts showing the lack of fractionation amongst the REE and Y with increasing total REE content. The *solid line* shows the Ce/Y ratios calculated for clinopyroxenes by the crystal fractionation model using the Wood and Bundy type model in Fig. 9 in which the Al dependence of D_o was calculated assuming local charge balance

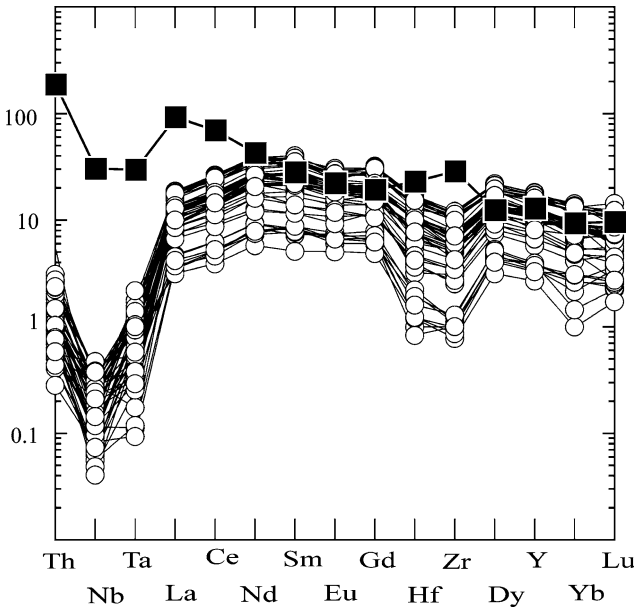

Fig. 11 Trace element profiles for Carmacks clinopyroxene phenocrysts (*open circles*) compared to the average trace element profile (*solid squares*) for Carmacks lavas with over 12 wt.% MgO; all normalized to C1 Carbonaceous Chondrite

phenocrysts strongly suggests the cyclic zoning of the clinopyroxenes reflects the repeated influx of primitive magma into a magma chamber containing relatively more evolved magma. Second, the behaviour of Sr and Th appear to be well reproduced using accepted partition coefficients, those for Th involving a strong Al^{IV} dependence that is supported by experimental data. Third, the trace element correlation with Al^{IV} abundance is repeated at least three times in each mantle of four clinopyroxene phenocrysts, suggesting a highly producible process. Finally, the mottled cores of the clinopyroxene phenocrysts appear to record a different history than the cyclically zoned mantles, yet the correlation between incompatible trace element abundance and Al concentration is indistinguishable from that observed in the clinopyroxene mantles.

Wood and Blundy's model (Wood and Blundy 2001) for the effect of Al on the partition coefficients for REE is based on distributed charge balance, a model that best fits the annealed experimental data. In such models, the REE^{3+} are not restricted to M2 sites adjacent to Al^{IV}, but are distributed across all cation sites in clinopyroxene, with the probabilities of individual site occupancies being determined by the lattice strain energies and electrostatic work that must be done to accommodate a REE^{3+} ion occupying them. The total REE^{3+} content of a clinopyroxene is the summation of all these partial site occupancies, and the predicted effect of Al^{IV} on REE partitioning is relatively

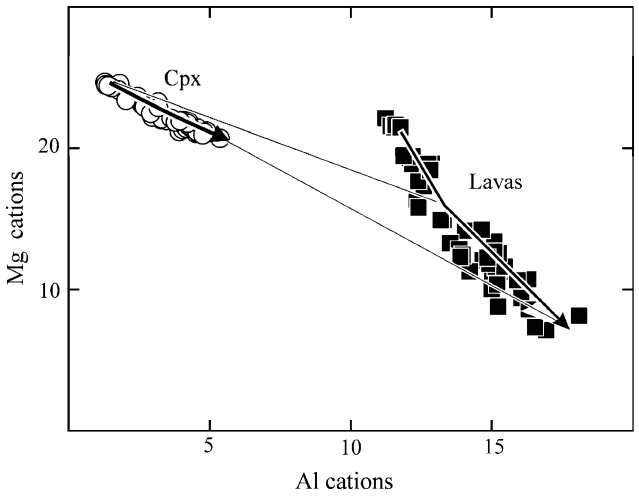

Fig. 12 Plot of Al versus Mg in cation units for the Carmacks clinopyroxene phenocrysts and the enclosing Carmacks lavas. The *solid arrows* indicate the calculated liquid line of descent and the corresponding clinopyroxenes calculated by removing olivine and clinopyroxene in instantaneous equilibrium with the liquid in steps of 0.1 wt.%. The olivine compositions were calculated using the algorithm of Beattie (1993) and the clinopyroxene compositions were calculated using the algorithm of (Nielson and Dungan 1983), with the Al content of clinopyroxene calculated using a $D_{Al} = 2.0 \times (e^{(23350/temp\ -\ 18.54)} \times Al)/(\sum network\ modifiers)$. The partition coefficients for all trace elements were recalculated at each step using the calculated liquid and clinopyroxene compositions

small (Wood and Blundy 2001). Models assuming local charge balance require the REE^{3+} to sit only in M2 sites that are directly adjacent to Al^{IV} substituting for Si^{4+}. Such a model predicts a much larger effect for Al^{IV} on REE^{3+} partitioning (Wood and Blundy 2001), and does in fact best reproduce the variations observed in the Carmacks clinopyroxene phenocrysts. The finely zoned nature of the Carmacks clinopyroxene phenocrysts clearly indicates that they have not been annealed. The fact that a local charge balance model for the Al^{IV} dependence of D_o better predicts the observed trace element variations may reflect the ease of attachment of 3^+ cations to M2 sites adjacent to Al^{IV} during crystal growth in natural systems, because of the electrostatic energy penalties associated with other cation sites in clinopyroxene.

The results of this study suggest that the effect of Al on the partition coefficients of incompatible trace elements in clinopyroxene is presently under appreciated in some natural systems. The zonation observed in the Carmacks clinopyroxene phenocrysts indicates that variations of as little as a few percent in Al can have a dramatic effect of the partition coefficients of these elements, with little fractionation between them. The differences between the observed results and experimentally predicted results may simply reflect the fact that local charge balance is a better model for crystal growth, whereas charge balance tends to become more distributed in annealed experiments designed to reach equilibrium.

Relatively extensive degrees of crystal fractionation are required for the effects of Al on the partitioning of incompatible trace elements in clinopyroxene to become evident in the residual liquids produced by crystal fractionation because of the low values of the partition coefficients and the low ratio of crystals to liquid. However, our models suggest that after as little as 20% crystal fractionation, elements such as Y and the HREE change from being incompatible to compatible in clinopyroxene (Fig. 11). The compositional dependence of trace element partitioning in clinopyroxene will cause more serious problems for compatible trace elements during crystal fractionation and for incompatible trace elements during partial melting, where the ratio of liquid to solid is low compared to the case for crystal fractionation in a magma chambers. Although a rigorous assessment of these effects during partial melting is beyond the scope of this paper, as an example, the Al content of the clinopyroxene of mantle xenoliths typically ranges from $\sim$7 wt.% Al_2O_3 in fertile lherzolites to $\sim$2.0 wt.% Al_2O_3 in refractory harzburgites (Shi et al. 1998), while Yb varies from 2 to 0.2 ppm. The variation in Yb is consistent with $\sim$25% partial melting, if a constant partition coefficient of 0.2 is assumed. In light of the results of this study, however, the variation of Al in the clinopyroxene would imply that the partition coefficients for Zr, Th, REE, and Y could be three times as large for the clinopyroxene of fertile lherzolites as for those of refractory harzburgites, which would have significant implications not only for the variation in trace element levels in melts at low degrees of partial melting, but for melt percolation phenomena in the mantle in general.

Conclusions

Although the partition coefficients of incompatible trace elements are known to be sensitive to the Al^{IV} contents of clinopyroxene (Wood and Blundy 2001), the results of our study suggest that the magnitude of this effect is under appreciated in some natural systems. The more than threefold increase in Th, Zr, REE and Y observed in the zoned clinopyroxene phenocrysts of the Carmacks ankaramites appears to reflect an increase in their partition coefficients with increasing Al^{IV} in the clinopyroxene. An increase from 1.5 to 4.0 wt.% Al_2O_3 during $\sim$20% crystal fractionation appears to be associated with more that a threefold increase partition coefficients of Th, Zr, REE, and Y. In contrast, the partition coefficient for Sr in the M2 site of clinopyroxene does not appear very sensitive to the aluminum content of the pyroxene. These variations are poorly reproduced by models in which the Al^{IV}

dependence of trace element partitioning in clinopyroxene assume distributed charge balance, but consistent with models assuming local charge balance. These findings suggest that caution may need to be exercised in applying experimentally determined partition coefficients to natural systems. Although extensive degrees of crystal fractionation are required for this effect to be detected in the residual liquids of crystal fractionation, it could cause more serious problems in modeling the behaviour of trace elements during partial melting and melt migration in the mantle, where the low liquid/solid ratios are likely to lead to significant melt chromatographic and melt structure (Gaetani 2004) effects.

Acknowledgments The authors would like to thank Lang Shi of the Electron Microprobe Laboratory for help with the electron microprobe analyses and Glenna Keating and Tariq Ahmedali of the Geochemical Laboratories for the X-ray fluorescence analyses. The ideas developed in this manuscript have benefited greatly from reviews by G. Gaetani, J. Blundy, and an anonymous reviewer. This research was supported by National Science and Engineering Research Council of Canada Discovery Grant No. RGPIN 7977-00. GEOTOP Publication No. 2007-0060.

References

Adam J, Green T (2006) Trace element partitioning between mica- and amphibole-bearing garnet lherzolite and hydrous melt: 1. Experimental results and the investigation of controls on partitioning behaviour. Contrib Mineral Petrol 152:1–17

Albarede F, Bottinga Y (1972) Kinetic disequilibrium in trace element partitioning between phenocrysts and host lava. Geochem Cosmochem Acta 36:141–156

Baker DR (1990) Chemical interdiffusion of dacite and rhyolite: anhydrous measurements at 1 atm and 10 kbar, application of transition state theory, and diffusion in zoned magma chambers. Contrib Mineral Petrol 104:407–423

Beattie P (1993) Olivine-melt and orthopyroxene-melt equilibria. Contrib Mineral Petrol 115:103–111

Blundy JD, Wood BJ (1991) Crystal-chemical controls on the partitioning of Sr and Ba between plagioclase feldspar, silicate melts, and hydrothermal solutions. Geochim Cosmochim Acta 55(1):193

Blundy JD, Wood BJ (1994) Prediction of crystal-melt partition coefficients from elastic moduli. Nature 372:452–454

Blundy J, Wood B (2003) Partitioning of trace elements between crystals and melts. Earth Planet Sci Lett 210(3):383–399

Blundy JD, Robinson JAC, Wood BJ (1998) Heavy REE are compatible in clinopyroxene on the spinel lherzolite solidus. Earth Planet Sci Lett 160:493–504

Bostock HS (1936) Carmacks district, Yukon. Geol Surv Can Memoir 189:67

Forsythe LM, Nielsen RL, Fisk MR (1994) High field strength element partitioning between pyroxene and basaltic to dacitic melts. Chem Geol 117:107–125

Gaetani GA (2004) The influence of melt structure on trace element partitioning near the peridotite solidus. Contrib Mineral Petrol 147:511–527

Gest DE, McBirney AR (1979) Genetic relationships of shoshonitic and absarokitic magmas, Absaroka Mountains, Wyoming. J Volcanol Geotherm Res 6:85–104

Hill E, Wood BJ, Blundy JD (2000) The effect of CaTschermaks component on trace element partitioning between clinopyroxene and silicate melt. Lithos 53:203–215

Johnston ST, Wynne PJ, Francis D, Hart CJR, Enkin RJ, Engebretson DC (1996) Yellowstone in Yukon: the late Cretaceous Carmacks group. Geology 24:997–1000

Lundstrom CC, Shaw HF, Ryerson FJ, Phinney DL, Gill JB, Williams Q (1994) Compositional controls on the partitioning of U, Th, Ba, Pb, Sr, and Zr between clinopyroxene and haplobasalts: implications for uranium series disequilibria in basalts. Earth Planet Sci Lett 128:407–423

Nielson RL, Dungan MA (1983) Low-pressure mineral melt equilibria in natural anhydrous mafic systems. Contrib Mineral Petrol 84:310–326

Putirka K, Johnson M, Kinzler R, Longhi J, Walker D (1996) Thermobarometry of mafic igneous rocks based on clinopyroxene-liquid equilibria, 0–30 kbars. Contrib Mineral Petrol 123:92–108

Putirka KD, Milkaelian H, Ryerson F, Shaw MH (2003) New clinopyroxene-liquid thermobarometers for mafic, evolved, and volatile-bearing lava compositions, with applications to lavas from Tibet and the Snake River Plain, Idaho. Am Mineral 88:1542–1554

Shi L, Francis D, Ludden J, Frederiksen A, Bostock M (1998) Xenolith evidence for lithospheric melting above anomalously hot mantle under the northern Canadian Cordillera. Contrib Mineral Petrol 131:39–53

Wood BJ, Blundy JD (1997) A predictive model for rare earth element partitioning between clinopyroxene and anhydrous silicate melt. Contrib Mineral Petrol 129:166–181

Wood BJ, Blundy JD (2001) The effect of cation charge on crystal-melt partitioning of trace elements. Earth Planet Sci Lett 188:59–71

Wood BJ, Trigila R (2001) Experimental determination of aluminous clinopyroxene-melt partition coefficients for potassic liquids, with applications to the evolution of the Roman province potassic magmas. Chem Geol 172:213–223